Reduction of ghost images of cervical vertebrae and intervertebral space in vertical dual-exposure panoramic radiography

Masao Kato

Nihon University Graduate School of Dentistry,

Major in Oral and Maxillofacial Radiology

(Directors: Prof. Yoshinori Arai and Assoc. Prof. Kunihito Matsumoto)

Contents

This thesis is based on the article listed below with additional data.

Kato M, Asakura S, Kimoto H, Sasaki T, Dezawa K, Amemiya T, Matsumoto K, Arai Y (2023) Reduction of ghost images of cervical vertebrae in panoramic radiography using vertical dual exposure. J Oral Sci (in press)

Summary

Intraoral radiography has been restricted in dental practice to reduce the risk of infection during the coronavirus disease 2019 pandemic. As an alternative, rotational panoramic radiography (PR) has been recommended. PR provides a tomographic image of both sides of the temporomandibular joint, maxillary sinus and the dental arch of the maxilla and mandible. X-rays pass through the cervical vertebrae (CV) and intervertebral space (IVS) when they create an image of the incisors. As a result, ghost images of the CV and IVS overlap with the image of the incisors. In particular, X-rays that have passed through the CV and IVS create blurred radiopaque and radiolucent ghost images, respectively. Because these ghost images are an obstacle to the diagnosis of periapical lesions and periodontal diseases, a new imaging modality as an alternative to intraoral radiography is needed to adequately evaluate incisor lesions in the pandemic. Therefore, the aim of this study was 1) to present a new vertical dual-exposure PR method that merges the images of two PRs taken at different heights to reduce CV and IVS ghost images in the incisor region in PR and 2) to evaluate the image quality of this dual-exposure PR method.

An aluminum block and a human CV immersed in a water bath, and a human head phantom with CV were used as imaging phantom. A Veraviewepox X550 was used for image acquisition. In this study, PR imaging was performed twice at half the exposure dose. The first PR image was collected in the normal position. For the second PR image, the heights of both the X-ray focus and the detector were increased by 0, 5, 10, 15, or 20 mm. The first and second PR images were taken in the normal position at a height of 0 mm ($PR^{1st}_{0\ mm}$ and $PR^{2nd}_{0\ mm}$, respectively). Images were also acquired at 5 mm ($PR_{5\ mm}$), 10 mm ($PR_{10\ mm}$), 15 mm ($PR_{15\ mm}$), and 20 mm ($PR_{20\ mm}$). A total of six PR images were acquired for each phantom. Custom software developed in C# was used to merge images by applying the least squares method. First, $PR^{1st}_{0\ mm}$ and $PR^{2nd}_{0\ mm}$ were merged ($Merg_{0\ +\ 0\ mm}$). Similarly, $PR^{1st}_{0\ mm}$ was merged with $PR_{5\ mm}$, $PR_{10\ mm}$, $PR_{15\ mm}$, or $PR_{20\ mm}$ and exported as $Merg_{0\ +\ 5\ mm}$, $Merg_{0\ +\ 10\ mm}$, $Merg_{0\ +\ 15\ mm}$, and $Merg_{0\ +\ 20\ mm}$, respectively. Next,

$PR^{1st}_{0\ mm}$ was subtracted from $PR^{2nd}_{0\ mm,}$ $PR_{5\ mm}$, $PR_{10\ mm}$, $PR_{15\ mm}$, or $PR_{20\ mm}$ to create $Sub_{0\ -\ 0\ mm}$, $Sub_{0\ -\ 5\ mm}$, $Sub_{0\ -\ 10\ mm}$, $Sub_{0\ -\ 15\ mm}$, and $Sub_{0\ -\ 20\ mm}$, respectively.

A line profile was extracted from the central part of the subtracted images the aluminum block phantom and from the center of the left mandibular central incisor in the subtracted images of the human head phantom. The intensity of the image pixels was analyzed as objective evaluation, and a histogram and standard deviation (SD) of the intensity values of the line profiles were obtained for all subtracted images. In the subjective image evaluation, six oral and maxillofacial radiologists selected the merged image in which the ghost CV and IVS images were less visible or the image intensity was more uniform. The number of selections was used as the score of each merged image. Subjective image evaluation was performed twice with an interval of 2 weeks. The mean scores of each rater were recorded and scores were compared between $Merg_{0\text{-}0\ mm}$ and other merged images using Wilcoxon signed-rank sum test. Intraclass coefficient (ICC) was calculated with 10 pairs of merged images to evaluate intra- and inter-rater reliability.

For aluminum block phantom, objective evaluation showed positional shift in the ghost images according to the height of the focus. The highest SD in the intensity values of the line profiles was observed in $Sub_{0\ -\ 10\ mm}$. In the subjective evaluation, the $Merg_{0\ +\ 0\ mm}$ obtained the worst score, indicating strong influence from the CV and IVS ghost images. In the subjective evaluation of the merged images, $Merg_{0\ +\ 0\ mm}$ obtained significantly worse score compared with other merged images ($P < 0.05$). The intra- and inter-rater reliability were respectively the mean ICC (1, 2) = 0.944 (range: 0.753-1.000) and ICC (2, 2) = 0.973. For human head phantom, objective evaluation showed positional shift in the ghost images according to the height of the focus. The highest SD in the intensity values of the line profiles was observed in $Sub_{0\ -\ 20\ mm}$. In the subjective evaluation of the merged images, $Merg_{0\ +\ 0\ mm}$ obtained significantly worse score compared with $Merg_{0\ +\ 5\ mm}$, $Merg_{0\ +\ 10\ mm}$ and $Merg_{0\ +\ 15\ mm}$ ($P < 0.05$). However, there was no statistically significant difference when comparing $Merg_{0\ +\ 0\ mm}$ to $Merg_{0\ +\ 20\ mm}$.

The intra- and inter-rater reliability were respectively the mean ICC (1, 2) = 0.719 (range: 0.304-1.000) and ICC (2, 2) = 0.732.

This study clearly demonstrated that the position of the CV and IVS ghost images shifted according to the change of the vertical position of the X-ray focus and detector in vertical dual-exposure PR. Consequently, the SD of the intensity value of the line profile on the incisor region varied. Subjective evaluation also showed less CV and IVS ghost images on the incisor area in $Merg_{0+5\ mm}$, $Merg_{0+10\ mm}$, $Merg_{0+15\ mm}$ and $Merg_{0+20\ mm}$ than in $Merg_{0+0\ mm}$. The vertical dual-exposure PR can reduce the ghost image and would become an alternative to intraoral radiography in incisor region.

Introduction

Intraoral radiography has been restricted in dental practice to reduce the risk of infection during the coronavirus disease 2019 pandemic. As an alternative, rotational panoramic radiography (PR) has been recommended [1-3]. Developed by Paatero [4,5], PR provides a tomographic image of both sides of the temporomandibular joint, maxillary sinus and the dental arch of the maxilla and mandible. X-rays pass through the cervical vertebrae (CV) and intervertebral space (IVS) when they create an image of the incisors. As a result, ghost images of the CV and IVS overlap with the image of the incisors. In particular, X-rays that have passed through the CV and IVS create blurred radiopaque and radiolucent ghost images, respectively. Finally, an image with non-uniform gradation is formed on the PR image [6-8]. These ghost images are an obstacle to the diagnosis of periapical lesions and periodontal diseases.

In the past, when it was difficult to make a diagnosis because of the overlap of the CV and IVS ghost images on the incisor region of the PR, intraoral radiography was added for confirmation. On this basis, a diagnosis could be made as to whether the cause of the non-uniform gradation was the CV ghost images or a lesion. However, additional intraoral radiography was not recommended when there was a risk of infection due to the pandemic [2,3].

Several authors have reported the usefulness of merging the images of dual imaging plate intraoral radiographs to improve image quality and reduce exposure dose [9-11], and it has been speculated that merging images would improve the adverse effects of ghost images in the incisor region in PR. The aim of this paper is 1) to present a new vertical dual-exposure PR method that merges the images of two PRs taken at different heights to reduce CV and IVS ghost images in the incisor region in PR and 2) to evaluate the image quality of this dual-exposure PR method.

Materials and Methods

Imaging phantoms

Two phantoms were used. The first consisted of an aluminum block 50 mm (H) × 20 mm (W) × 10 mm (D) in size and a human CV immersed in a water bath 17 cm in diameter (Fig. 1a). The second was a human head phantom with CV (Fig. 1b: SE-2, Osaka Kasei Co., Osaka, Japan).

PR imaging using the dual-exposure PR method

A Veraviewepox X550 (J. Morita Co., Kyoto, Japan), digital PR system based on a charged-coupled device (CCD) [12,13], was used for image acquisition. The bottom surface of the water bath for the aluminum block phantom imaging and the Frankfurt horizontal plane of the human head phantom were set parallel to the floor. The exposure conditions of the PR were as follows: the exposure time was 17 s, the tube voltage was 80 kV, and the pixel size was 0.099 mm × 0.099 mm. The tube current was set to 5 mA, which was half the value used in daily PR imaging for patients. In this study, PR imaging was performed twice at half the exposure dose. The first PR image was collected in the normal position. For the second PR image, the heights of both the X-ray focus and the detector were increased by 0, 5, 10, 15, or 20 mm. Figure 2 shows the relative positions of the X-ray focus, CV, maxillary incisors, and detector when the maxillary incisors were imaged using PR. Finally, the position of the ghost image of the CV and IVS on the incisors is shifted downward.

The first and second PR images were taken in the normal position at a height of 0 mm ($PR^{1st}_{0\ mm}$ and $PR^{2nd}_{0\ mm}$, respectively) . Images were also acquired at 5 mm ($PR_{5\ mm}$), 10 mm ($PR_{10\ mm}$), 15 mm ($PR_{15\ mm}$), and 20 mm ($PR_{20\ mm}$). A total of six PR images were acquired for each phantom.

Image processing in the vertical dual-exposure PR method

Custom software developed in C# (Microsoft, Redmond, WA, USA) was used to merge images by applying the least squares method [14-18]. First, $PR^{1st}_{0\ mm}$ and $PR^{2nd}_{0\ mm}$ were merged ($Merg_{0+0\ mm}$). Similarly, $PR^{1st}_{0\ mm}$ was merged with $PR_{5\ mm}$, $PR_{10\ mm}$, $PR_{15\ mm}$, or $PR_{20\ mm}$ and exported as $Merg_{0+5\ mm}$, $Merg_{0+10\ mm}$, $Merg_{0+15\ mm}$, and $Merg_{0+20\ mm}$, respectively, for subjective image analysis. Next, $PR^{1st}_{0\ mm}$ was subtracted from $PR^{2nd}_{0\ mm}$, $PR_{5\ mm}$, $PR_{10\ mm}$, $PR_{15\ mm}$, or $PR_{20\ mm}$ to create $Sub_{0-0\ mm}$, $Sub_{0-5\ mm}$, $Sub_{0-10\ mm}$, $Sub_{0-15\ mm}$, and $Sub_{0-20\ mm}$, respectively, for objective image analysis. All merged and subtracted images were exported as 8-bit grayscale bitmaps.

Objective image analysis

A line profile 579 pixels in length was extracted from the central part of the subtracted images and used to depict the aluminum block phantom. A line profile 389 pixels in length was extracted from the center of the left mandibular central incisor in the subtracted images of the human head phantom. The intensity of the image pixels was analyzed using custom software written in C#. Finally, a histogram of the intensity values of the line profiles was obtained for all subtracted images.

Subjective image evaluation

Six oral and maxillofacial radiologists evaluated the images using viewing software developed in C# that randomly displayed a pair of merged images, e.g., $Merg_{0+10\ mm}$ vs. $Merg_{0+15\ mm}$. Although this study only required a comparison between $Merg_{0+0\ mm}$ and the other merged images, all combinations of merged images (10 pairs) were evaluated by each rater to ensure both the fairness of the evaluation and the reliability of the image evaluation. The raters selected the merged image in which the ghost CV and IVS images were less visible or the image intensity was more uniform. The number of selections was used as the score of each merged image. No information about the settings of the merged images was presented to the raters for the evaluation. A liquid crystal display monitor

(3,840 × 2,160 pixels; MultiSync LCD-EA271U, NEC, Tokyo, Japan) was used for evaluation. Subjective image evaluation was performed twice with an interval of 2 weeks. The mean scores of each rater were recorded. The median of the scores of all six raters was defined as the representative value of each merged image.

Statistical analysis

In the subjective evaluation, scores were compared between $Merg_{0\text{-}0\ mm}$ and other merged images using Wilcoxon signed-rank sum test (n = 6). Intraclass coefficient (ICC) was calculated with 10 pairs of merged images to evaluate intra- and inter-rater reliability [19]. The median ICC for intra-rater reliability evaluation for each rater was noted. ICC values less than 0.5, between 0.50 and 0.75, between 0.75 and 0.90, and greater than 0.90 were interpreted as poor, moderate, good, and excellent reliability, respectively [20]. The above analysis was performed for each phantom using Microsoft Excel for Mac ver. 16.75 (Microsoft) and SPSS (IBM Corp., New York, NY, USA). A P value less than 0.05 was considered to indicate a statistically significant difference.

Results

Aluminum block and CV phantom

Figure 3 shows the PRs at each height and merged and subtracted images of the aluminum block and CV phantom. Ghost images of the CV and IVS were observed in all PR and merged images. Random noise was observed in $Sub_{0\ -\ 0\ mm}$ (Fig. 3). In $Sub_{0\ -\ 5\ mm}$, $Sub_{0\ -\ 10\ mm}$, $Sub_{0\ -\ 15\ mm}$, and $Sub_{0\ -\ 20\ mm}$, the ghost images of CV and IVS showing black-and-white patterns such as blurred checkerboards were shifted vertically (Fig. 3). The frequency distribution and standard deviation of the pixel intensities of the line profile of each subtracted image are shown in Fig. 4 and Table 1, respectively.

In the subjective evaluation of the merged images, $Merg_{0\ +\ 0\ mm}$ obtained significantly worse score compared with other merged images ($P < 0.05$; Table 2), which indicates that

the ghost images were reduced in $Merg_{0+5\ mm}$, $Merg_{0+10\ mm}$, $Merg_{0+15\ mm}$, and $Merg_{0+20\ mm}$. The intra- and inter-rater reliability were respectively the mean ICC (1, 2) = 0.944 (range: 0.753-1.000) and ICC (2, 2) = 0.973.

Human head phantom

Figure 5 shows the PRs at each height. Merged and subtracted images of the human head and CV phantom are shown. The frequency distribution and standard deviation of the pixel intensities of the line profile through the center of the left mandibular central incisor are shown in Fig. 6 and Table 1, respectively. In the subjective evaluation of the merged images, $Merg_{0+0\ mm}$ obtained significantly worse score compared with $Merg_{0+5\ mm}$, $Merg_{0+10\ mm}$ and $Merg_{0+15\ mm}$ ($P < 0.05$; Table 2). However, there was no statistically significant difference when comparing $Merg_{0+0\ mm}$ to $Merg_{0+20\ mm}$. The intra- and inter-rater reliability were respectively the mean ICC (1, 2) = 0.719 (range: 0.304-1.000) and ICC (2, 2) = 0.732.

Discussion

The CV are exposed three times during PR imaging [5-8,12,13]: the X-rays are projected twice laterally from the left and right sides of the CV behind the mandible, and when imaging the incisors, the X-rays are projected posteroanteriorly from the back of the head. The X-rays pass through the CV and are then projected onto the incisor region. Since the CV are far from the tomographic layer, they overlap the PR images of the incisor as a horizontally blurred ghost image. The CV and IVS ghost images in the incisor region appear as radiopacity and radiolucency, respectively. The magnification of the ghost images of the IVS during imaging of incisor region can be calculated using the following formula (see Fig. 2):

$$\text{magnification of the IVS ghost image in the incisor region} = \frac{CVI+FCV}{FCV}$$

Here, CVI is the distance between the CV and incisor and FCV is the distance between the focus and CV.

If the IVS distance is 3 mm, the projected size of ghost image of the IVS will be magnified approximately 1.38 times to 4.1 mm in the incisor region. In cases where strong ghost images occur in the incisor region, lesions can be overlooked and misdiagnosis can occur. To solve this problem, two images taken at different heights were merged to obscure ghost images in PR images. One PR image was taken at the normal position and the other image was with height of the X-ray focus increased. Then, the position of the ghost images was shifted downward in the incisor region. When the X-ray focus was elevated, as shown in Fig. 2, the IVS ghost image was projected inferiorly on the maxillary incisors. The amount of shift of the ghost image in the maxillary incisor region (SGoI) can be calculated from the distance between the maxillary incisors, the CV, or the X-ray focus as in the formula below.

$$\mathrm{SGoI} = \frac{\mathrm{CVI}}{\mathrm{FCV}} \times \mathrm{ARF}$$

Here, ARF represents the amount of raise of the X-ray focus.

If the X-ray focus is raised by 5 mm, the ghost images of the IVS in the incisor will be displaced inferiorly by approximately 1.9 mm. Moreover, if the X-ray focus is elevated by 11.79 mm or more, the shift in the ghost image may exceed the width of the IVS.

In this study, a line profile was used to evaluate the increase or decrease in the visibility of the ghost image. The CV and IVS ghost image overlapping the incisor region is unclear in the horizontal direction because it is far from the tomographic layer. Objective image analysis for both aluminum block and human head phantoms showed discrepancies in the frequency of the intensity value of the line profile on each subtracted image. On the other hand, the uniformity in the ghost images increased with shifting

heights of X-ray focus. These results suggest that raising the X-ray focus makes it possible to shift the position of the ghost image in the incisor region and indicates that ghost images can be improved by merging two images taken at different heights in PR.

In the subjective image evaluation, the score of $Merg_{0+0\,mm}$ was the worst and $Merg_{0+20\,mm}$ obtained the highest score for both phantoms (this was not statistically evaluated). These results also suggest that raising the X-ray focus and merging two PR images can reduce the ghost images of the CV and IVS. If the X-ray focus is elevated too much, the geometric distortion of the image will increase. If the difference between the 0 mm PR image and the upshifted PR image becomes too large, blur may occur because the least squares method may not converge [11]. Therefore, it is better to elevate the X-ray focus as little as possible. In the subtracted images of the human head phantom (Fig. 5), the outlines of the teeth are clearly observed in the subtracted image, especially in $Sub_{0-20\,mm}$. This is due to geometric distortion caused by a large shift in the X-ray focus.

The vertical dual-exposure PR method requires both the initial image as well as a second image with the X-ray focus shifted upward. The radiation dose is doubled when the normal exposure conditions are used in the vertical dual-exposure PR method. Therefore, to make the exposure dose equivalent to that of the normal PR imaging conditions, the vertical dual-exposure PR method uses half the normal tube current for each exposure. In this way, an increase in the exposure dose, even with two exposures can be avoided in the vertical dual-exposure PR method. In normal PR exposure conditions, the X-ray tube current is about 10 mA, but it was set to 5 mA in the vertical dual-exposure PR method. Theoretically, the milliampere-seconds of normal PR exposure at 10 mA and two PR exposures at 5 mA are equivalent. In clinical practice, collecting two PR images contributes to some clinical problems for patients and staff such as prolonged examination time. In addition, a good merged image may not be possible because of the increased risk of body motion and shifts in the head position due to the extension of the imaging time. Therefore, for clinical application, it is considered

necessary to fix the patient and improve the method of image fusion.

This study had a serious limitation in that the optimal amount of increase in the X-ray focus height was not evaluated due to the limited number of phantoms. CVI, FCV, and IVS vary according to patient. Therefore, these data cannot be directly applied in clinical settings. In this study, the optimal increase in the X-ray focus height was determined by calculating the thickness of the IVS as well as the distances between the focus, CV, incisors, and detector. Because the thickness of the IVS of each patient cannot be obtained directly using the vertical dual-exposure PR method, there is no choice but to infer the optimal increase using the anatomical average. The PR system used in this study was a CCD system [12,13] and does not have tomosynthesis capabilities. Therefore, the tomographic layer could not be moved after imaging. A PR system equipped with the latest tomosynthesis function would be able to move the tomographic layer [21-24]. Using tomosynthesis, it could be possible to correct the displacement of the image due to the patient's body movement. This distance can vary greatly depending on the structure and inclination of the CV of individuals. For practical application, a mechanism in PR is required that can determine the optimal amount of elevation by determining the distances between IVSs. In addition, vertical dual-exposure PR method has the following challenges to overcome for its application in clinical practice: extension of imaging time for two exposure, extension of image processing time to create a merged PR image, and need of instrument to firmly fix patients head, positioning tool such as chin rest for responding to change of exposure height, and to correct the magnification rate of incisors accompanied by a change of X-ray focus. Future studies should also clarify whether reduction of ghost images by vertical dual-exposure PR method can actually improve diagnostic accuracy of dental caries, periodontal and periapical disease of the incisors.

Conclusions

1) The position of the CV and IVS ghost images projected on the incisor region shifted according to the change of the vertical position of the X-ray focus and detector.
2) The profile and standard deviation of the intensity value of the line profile varied corresponding to the vertical position of the X-ray focus and detector.
3) Subjective evaluation showed less CV and IVS ghost images on the incisor area in $Merg_{0+5\ mm}$, $Merg_{0+10\ mm}$, $Merg_{0+15\ mm}$ and $Merg_{0+20\ mm}$ than in $Merg_{0+0\ mm}$.
4) The vertical dual-exposure PR method, which can produce a merged PR image of the normal position and the elevated X-ray focus, can reduce the ghost image and would become an alternative to intraoral radiography in incisor region.

References

1. Hamedani S, Farshidfar N (2020) The practice of oral and maxillofacial radiology during COVID-19 outbreak. Oral Radiol 36, 400-403.
2. Little R, Howell J, Nixon P (2020) COVID-19 and beyond: Implications for dental radiography. Br Dent J 229, 105-109.
3. MacDonald DS, Colosi DC, Mupparapu M, Kumar V, Shintaku WH, Ahmad M (2021) Guidelines for oral and maxillofacial imaging: COVID-19 considerations. Oral Surg Oral Med Oral Pathol Oral Radiol 131, 99-110.
4. Paatero YV (1949) A new tomographical method for radiographing curved outer surfaces. Acta Radiol 32, 177-184.
5. Paatero YV (1954) Pantomography in theory and use. Acta Radiol 41, 321-335.
6. McDavid WD, Langlais RP, Welander U, Morris CR (1983) Real, double, and ghost images in rotational panoramic radiography. Dentomaxillofac Radiol 12, 122-128.
7. Kaugars GE, Collett WK (1987) Panoramic ghosts. Oral Surg Oral Med Oral Pathol 63, 103-108.
8. Reuter I, Ritter W, Kaeppler G (1999) Triple images on panoramic radiographs. Dentomaxillofac Radiol 28, 316-319.
9. Watanabe K, Imanishi Y, Kato M, Kimoto H, Sekiguchi T, Amemiya T, Dezawa K, Matsumoto K, Arai Y (2022) Preliminary evaluation of dual imaging plate intraoral radiography. J Oral Sci 64, 69-73.
10. Imanishi Y, Sekiguchi T, Kato M, Kimoto H, Amemiya T, Dezawa K, Matsumoto K, Arai Y (2023) Reduction of scratch or dirt artifacts on intraoral radiographs using dual imaging plates in image processing. Oral Radiol 39, 386-393.
11. Sekiguchi T, Kato M, Kimoto H, Amemiya T, Dezawa K, Imanishi Y, Matsumoto K, Arai Y (2023) Correction of intraoral radiography with dual imaging plates

using enlargement of the horizontal direction with division into 12 blocks. J Oral Sci 65, 40-43.

12. Farman AG, Farman TT (1998) Panoramic dental radiography using a charge-coupled device receptor. J Digit Imaging 11, 166-168.
13. Farman TT, Farman AG (1998) Clinical trial of panoramic dental radiography using a ccd receptor. J Digit Imaging 11, 169-171.
14. Yamane R (1992) Basic study of one-shot dual energy subtraction sialography. Oral Radiol 8, 11-19.
15. Matsuki T (1994) Basic study of one-shot dual-energy subtraction sialography: (iii) fundamental study of contrast media. Oral Radiol 10, 55-62.
16. Workman A, Cowen AR (1995) Improved image quality utilizing dual plate computed radiography. Br J Radiol 68, 182-188.
17. Tsuda N, Tanaka N, Akasaka T, Yabuuchi H, Morishita J (2014) Dose reduction in general radiography for adult patients by use of a dual-side-reading photostimulable phosphor plate in a computed radiography system. Radiol Phys Technol 7, 310-315.
18. Minato K, Yamazaki M, Yagi T, Hirata T, Tominaga M, You K, Ishikawa H (2023) Effectiveness of one-shot dual-energy subtraction chest radiography with flat-panel detector in distinguishing between calcified and non-calcified nodules. Sci Rep 13, 9548.
19. Hallgren KA (2012) Computing inter-rater reliability for observational data: An overview and tutorial. Tutor Quant Methods Psychol 8, 23-34.
20. Koo TK, Li MY (2016) A guideline of selecting and reporting intraclass correlation coefficients for reliability research. J Chiropr Med 15, 155-163.
21. Webber RL, Horton RA, Tyndall DA, Ludlow JB (1997) Tuned-aperture computed tomography (TACT). Theory and application for three-dimensional dento-alveolar imaging. Dentomaxillofac Radiol 26, 53-62.

22. Ogawa K, Langlais RP, McDavid WD, Noujeim M, Seki K, Okano T, Yamakawa T, Sue T (2010) Development of a new dental panoramic radiographic system based on a tomosynthesis method. Dentomaxillofac Radiol 39, 47-53.
23. Noujeim M, Prihoda T, McDavid WD, Ogawa K, Yamakawa T, Seki K, Okano T, Sue T, Langlais RP (2011) Pre-clinical evaluation of a new dental panoramic radiographic system based on tomosynthesis method. Dentomaxillofac Radiol 40, 42-46.
24. Jeon KJ, Han SS, Lee C, Choi YJ, Jung HI, Kim YH (2020) Application of panoramic radiography with a multilayer imaging program for detecting proximal caries: A preliminary clinical study. Dentomaxillofac Radiol 49, 20190467.

Tables and Figures

Table 1 Standard deviation of image density value of the line profile on subtracted images

	Aluminum block and cervical vertebrae phantom	Human head phantom
$Sub_{0 - 0\ mm}$	5.4	1.7
$Sub_{0 - 5\ mm}$	9.8	5.3
$Sub_{0 - 10\ mm}$	12.2	6.2
$Sub_{0 - 15\ mm}$	11.5	7.8
$Sub_{0 - 20\ mm}$	9.9	9.4

Table 2 Score of the subjective image evaluation by six raters

	Aluminum block and cervical vertebrae phantom		Human head phantom	
	median	interquartile range	median	interquartile range
$Merg_{0+0\ mm}$	0.00 *	0.00	0.25 *	0.50
$Merg_{0+5\ mm}$	1.00	0.00	2.00	0.75
$Merg_{0+10\ mm}$	3.00	0.00	2.25	1.25
$Merg_{0+15\ mm}$	2.25	0.88	2.50	0.75
$Merg_{0+20\ mm}$	3.75	0.50	2.75	2.25

Median was calculated with the average score in two times of evaluation by each rater. Scores were compared between $Merg_{0\text{-}0\ mm}$ and other merged images using Wilcoxon signed-rank sum test. * $P < 0.05$

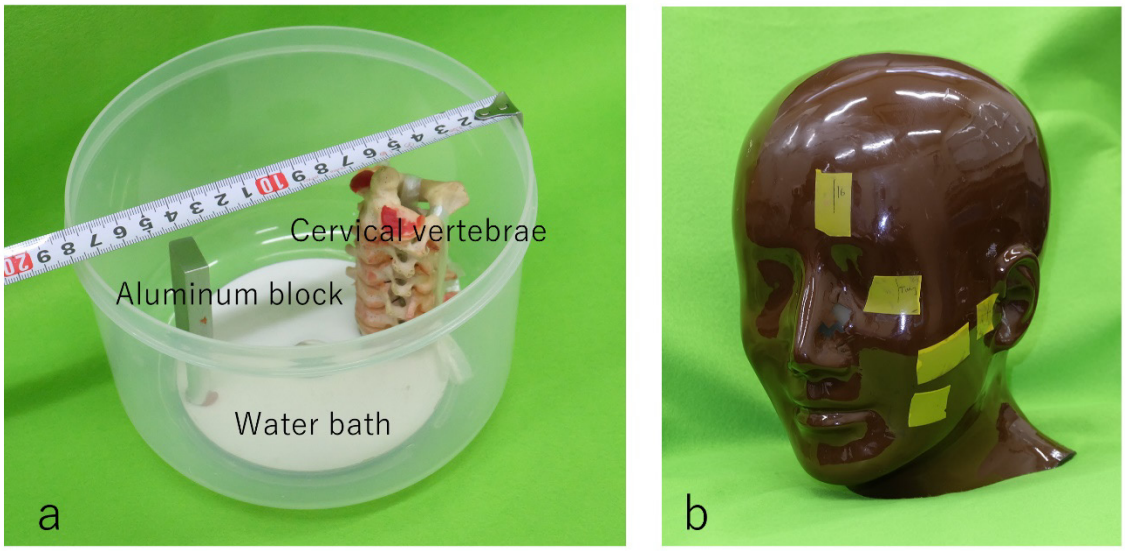

Fig. 1 Overview of the phantoms

a, aluminum block phantom with cervical vertebrae; b, human head phantom

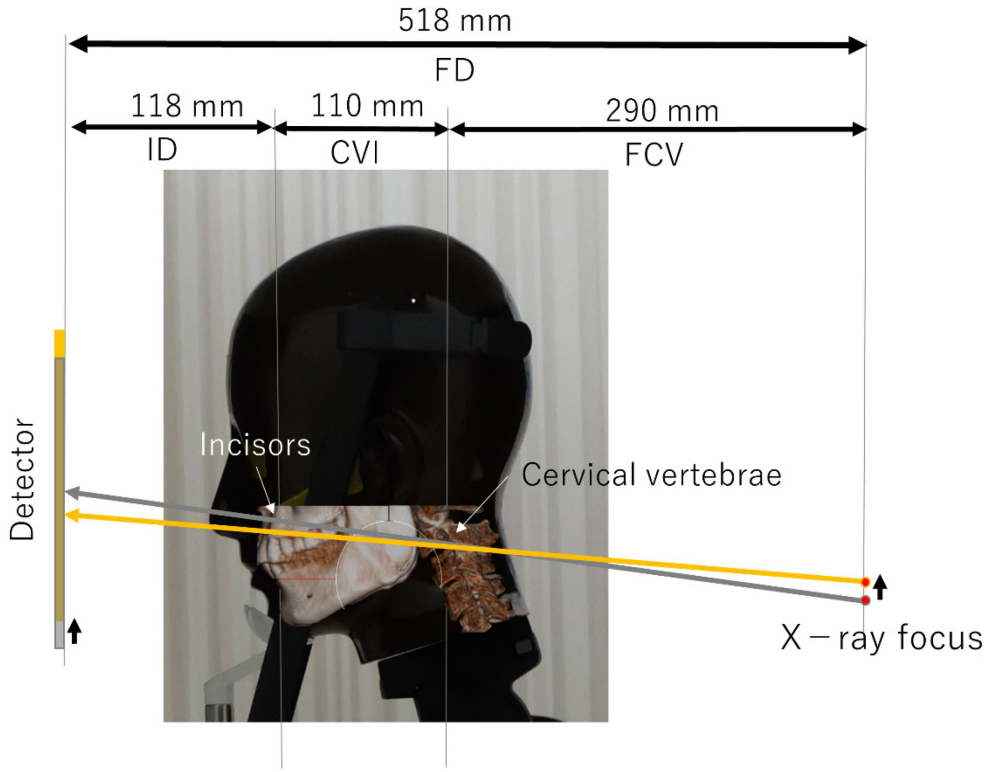

Fig. 2

The relative positions of the X-ray focal point, cervical vertebrae, and detector when imaging the incisor region in panoramic radiography

In general, the X-ray beam in panoramic radiography has a superoinferior tilt (gray arrow) and is projected onto the cervical vertebrae, incisor area, and detector (gray detector). When the X-ray focal point and detector (yellow detector) are raised, the projected angle of the X-ray beam (yellow arrow) onto the incisor area is changed and the ghost image of the cervical vertebrae is shifted downward with respect to the incisors and detector.

FD, distance from the focal point to the detector; ID, distance from the incisors to the detector; CVI, distance from the cervical vertebrae to the incisors; FCV, distance from the focal point to the cervical vertebrae

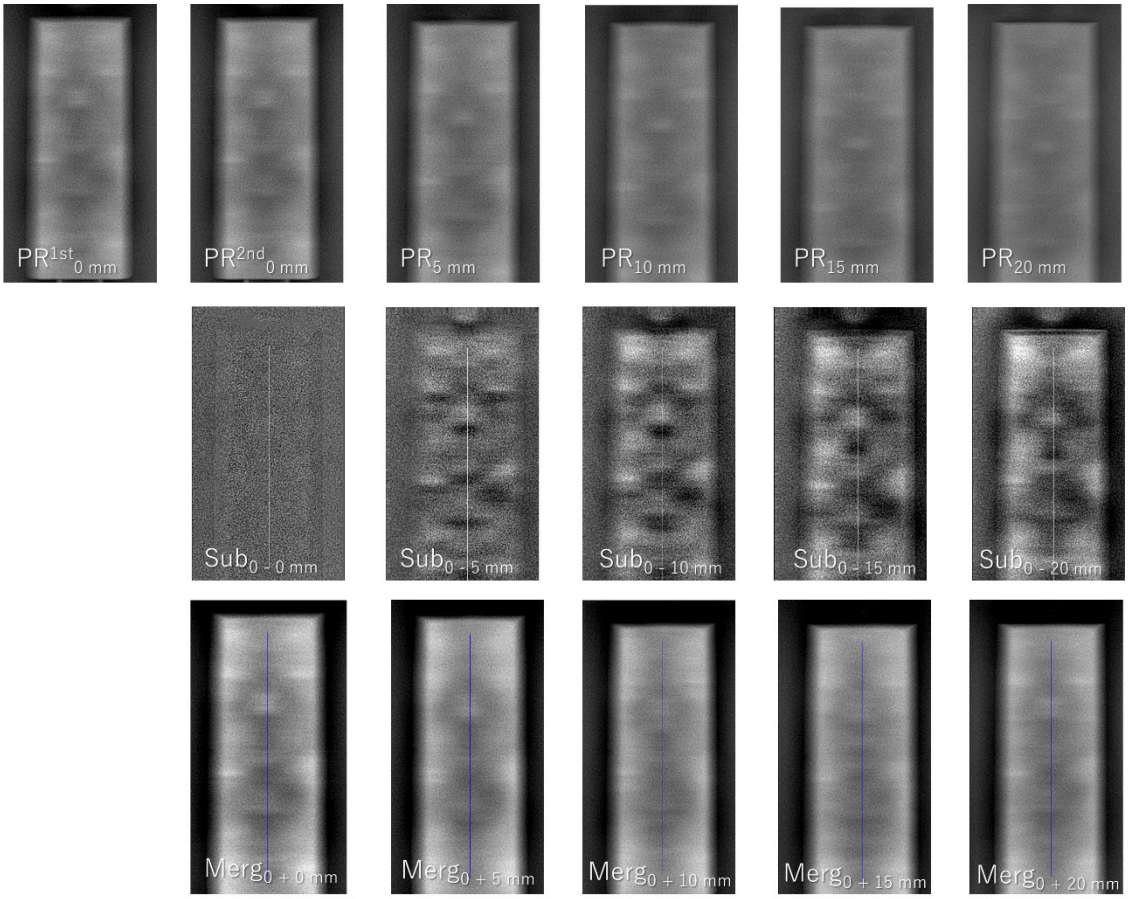

Fig. 3 Panoramic radiographs taken at different heights, and the merged and subtracted images of the aluminum block and cervical vertebrae phantom

$PR_{0\ mm}$, $PR_{5\ mm}$, $PR_{10\ mm}$, $PR_{15\ mm}$, and $PR_{20\ mm}$ were acquired at the normal position and at heights of 5 mm, 10 mm, 15 mm, and 20 mm, respectively. $PR_{0\ mm}$ was collected twice. Images $PR^{1st}{}_{0\ mm}$ and $PR^{2nd}{}_{0\ mm}$, $PR^{1st}{}_{0\ mm}$ and $PR_{5\ mm}$, $PR^{1st}{}_{0\ mm}$ and $PR_{10\ mm}$, $PR^{1st}{}_{0\ mm}$ and $PR_{15\ mm}$, and $PR^{1st}{}_{0\ mm}$ and $PR_{20\ mm}$ were merged to create $Merg_{0+0\ mm}$, $Merg_{0+5\ mm}$, $Merg_{0+10\ mm}$, $Merg_{0+15\ mm}$ and $Merg_{0+20\ mm}$, respectively. Similarly, the subtracted images $Sub_{0-0\ mm}$, $Sub_{0-5\ mm}$, $Sub_{0-10\ mm}$, $Sub_{0-15\ mm}$ and $Sub_{0-20\ mm}$ were also created.

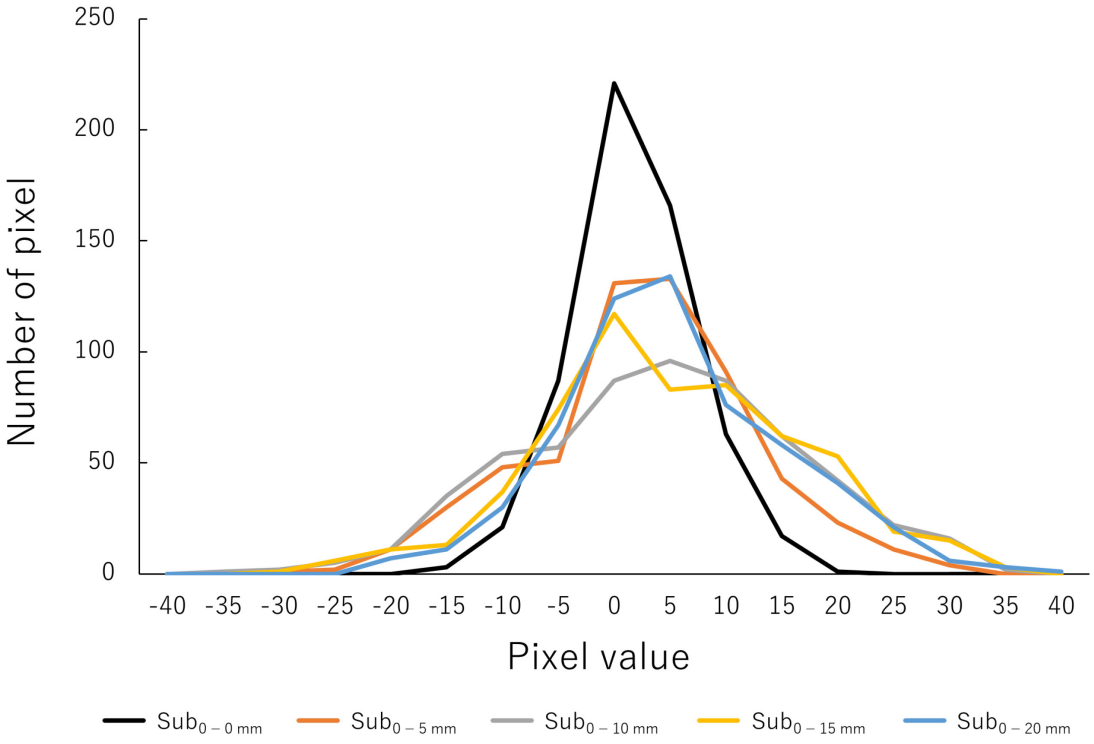

Fig. 4 Frequency distribution of the pixel intensities in the line profile of each subtracted image of the aluminum block and cervical vertebrae phantom

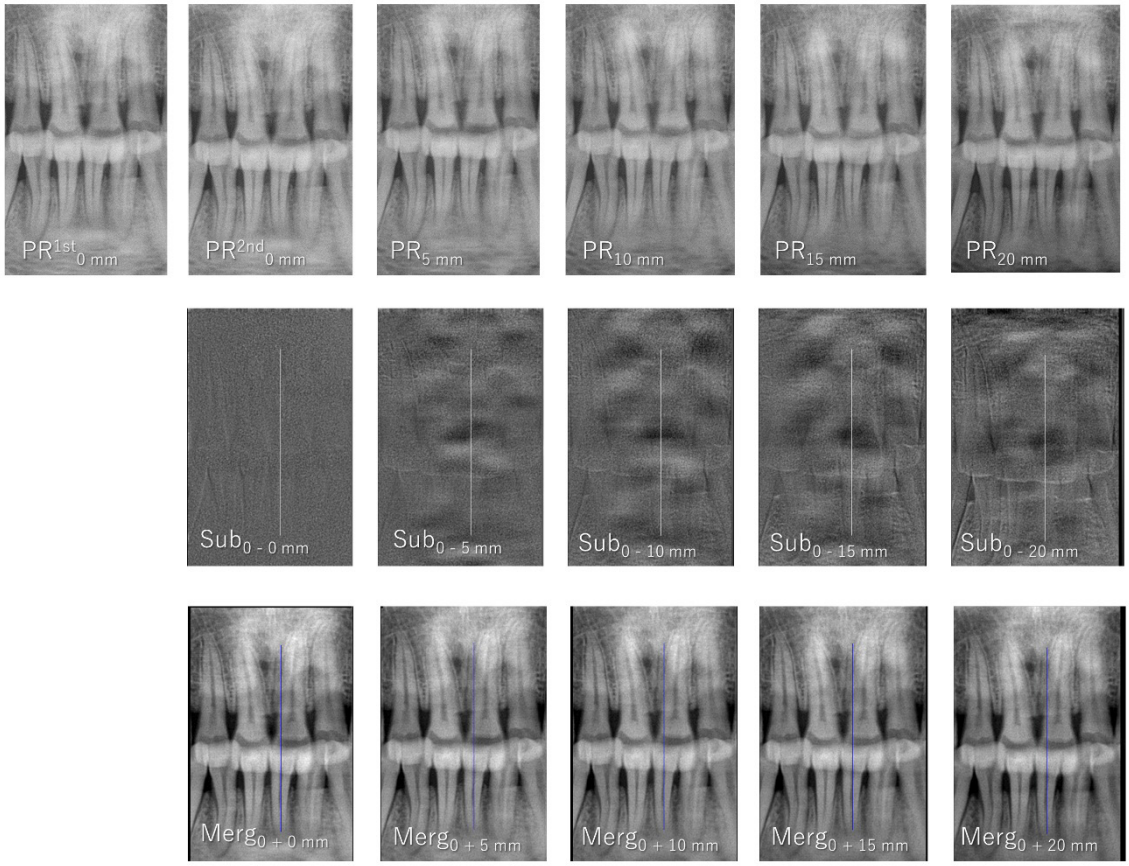

Fig. 5 Panoramic radiographs taken at each height and the merged and subtracted images of the human head phantom

$PR_{0\ mm}$, $PR_{5\ mm}$, $PR_{10\ mm}$, $PR_{15\ mm}$, and $PR_{20\ mm}$ were acquired at the normal position and at heights of 5 mm, 10 mm, 15 mm, and 20 mm, respectively. $PR_{0\ mm}$ was collected twice. Images $PR^{1st}{}_{0\ mm}$ and $PR^{2nd}{}_{0\ mm}$, $PR^{1st}{}_{0\ mm}$ and $PR_{5\ mm}$, $PR^{1st}{}_{0\ mm}$ and $PR_{10\ mm}$, $PR^{1st}{}_{0\ mm}$ and $PR_{15\ mm}$, and $PR^{1st}{}_{0\ mm}$ and $PR_{20\ mm}$ were merged to create $Merg_{0\ +\ 0\ mm}$, $Merg_{0\ +\ 5\ mm}$, $Merg_{0\ +\ 10\ mm}$, $Merg_{0\ +\ 15\ mm}$ and $Merg_{0\ +\ 20\ mm}$, respectively. Similarly, the subtracted images $Sub_{0\ -\ 0\ mm}$, $Sub_{0\ -\ 5\ mm}$, $Sub_{0\ -\ 10\ mm}$, $Sub_{0\ -\ 15\ mm}$ and $Sub_{0\ -\ 20\ mm}$ were also created.

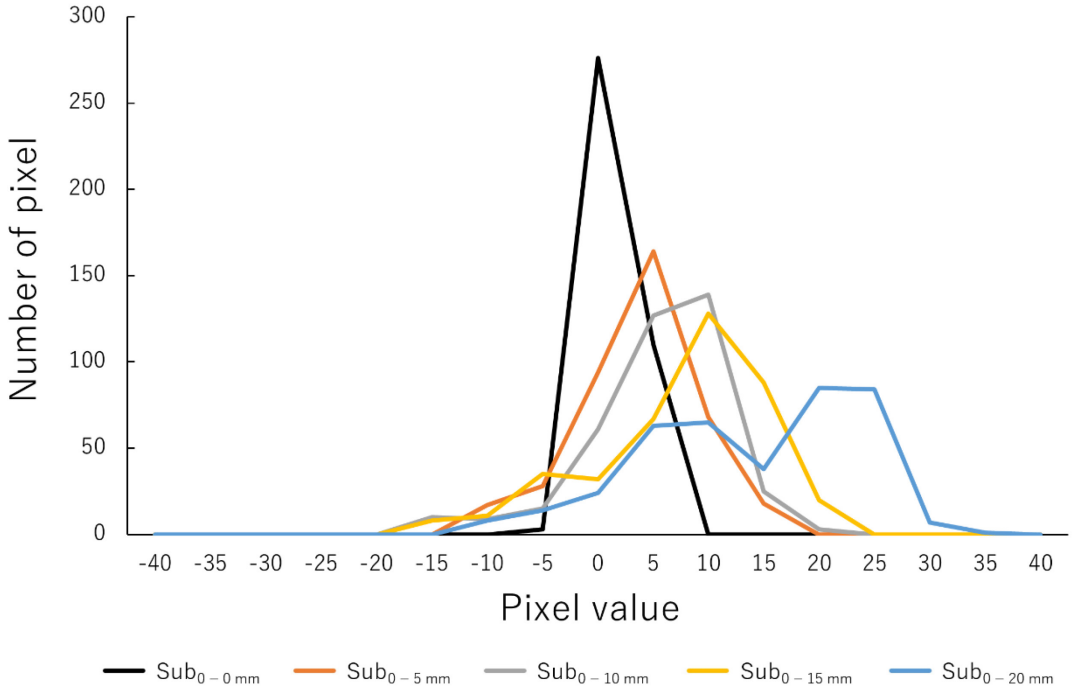

Fig. 6 Frequency distribution of the pixel intensities in the line profile of each subtracted image of the human head phantom